Epitaxial growth of graphene on Ir(111) by liquid precursor deposition

Frank Müller,[1,*] Samuel Grandthyll,[1] Christian Zeitz,[1] Karin Jacobs,[1] Stefan Hüfner,[1] Stefan Gsell,[2] and Matthias Schreck[2]
[1]*Experimental Physics, Saarland University, D-66123 Saarbrücken, Germany*
[2]*Institute of Physics, University of Augsburg, D-86135 Augsburg, Germany*
(Received 6 May 2011; published 12 August 2011)

The epitaxial growth of graphene on the surface of an Ir/YSZ/Si(111) multilayer substrate via the deposition of a liquid carbon precursor (acetone) was investigated by x-ray photoelectron spectroscopy, x-ray photoelectron diffraction, low-energy electron diffraction (LEED), and Fermi surface mapping. It is shown that the onset of graphene formation starts in a low temperature range around 600 K and that subsequent annealing up to 1000 K finally results in well-ordered graphene monolayers. Comparison of temperature-dependent LEED data with model calculations suggests that the growth of graphene takes place via a backbonelike growth by the formation of a hexagonal network connecting the hcp and fcc configuration sites within the $\sim 10 \times 10/9 \times 9$ supercell. In LEED, the low intensities of the superstructure related satellite spots give evidence for only small corrugations of the graphene layer due to weak interaction with the Ir(111) surface, making graphene on Ir(111) similar to free-standing graphene with the Fermi surface providing distinct spots at the *K* points.

DOI: 10.1103/PhysRevB.84.075472 PACS number(s): 68.65.Pq, 61.46.−w, 68.55.A−, 81.16.Dn

I. INTRODUCTION

In an early study by Wallace[1] the band structure of a "single hexagonal layer" of graphite (nowadays known as graphene) was calculated in the tight-binding ansatz, revealing a linear energy dispersion close to the so-called Dirac point at the corners of the Brillouin zone and predicting nearly massless electrons close to the Fermi energy. More than half a century later, the *"rise of graphene"*[2] started when it became possible to extract single layers from graphite by successive cleavage of highly oriented pyrolytic graphite crystals[3] and, soon afterward, graphene-based nanotransistors were demonstrated.[4] Properties, such as a very high mobility of the charge carriers and ballistic transport in the range of several hundred nanometers or larger,[2] qualify graphene as a promising material to replace silicon in future nanoelectronic devices. To reach this aim, the development of a technique for controlled preparation of graphene layers over large areas represents one of the most crucial steps. Currently, epitaxial graphene layers on single crystal surfaces provide the most promising concept.[2] One intensively studied example is based on the selective desorption of silicon from a SiC surface.[5] This system profits from the fact that the carbon layer is automatically placed on top of an insulator when a highly resistive SiC substrate is used for the experiments.

Apart from electronic aspects, there are also other fields of application for which epitaxial graphene even on a metal surface is of particular interest, as, e.g., in nanotribology. The precision of micromechanical devices, such as positioning systems, will increase as friction decreases. Compared to the bare substrate surface, the presence of single-layer graphene leads to a strong reduction of friction, as recently shown for epitaxial graphene on a SiC surface.[6] However, single-layer graphene is not the optimum choice as a lubricant since friction can be further reduced by bilayer graphene[6] or even multilayer graphene.[7] The outperforming of multilayer graphene is explained by the larger stiffness compared to single layers making multilayer films less able to adapt the topography of the surface.[8] Apart from the overall reduction of friction, even frictional anisotropies, as reported for graphite,[9] offer some potential with respect to a kind of self-alignment in case that friction is small along the direction of movement but larger perpendicular to it.

A second route towards epitaxial graphene is based on epitaxial growth on metal surfaces. It is typically done by chemical vapour deposition (CVD) using carbon-containing precursors, such as ethene (ethylene) (C_2H_4),[10–12] acetylene (C_2H_2),[13] or methane (CH_4).[14] In an even simpler way carbon dissolved as an impurity in the metal lattice segregates to the surface and forms graphene.[15] A thorough review of epitaxial graphene on transition metal (TM) surfaces was published by Wintterlin and Bocquet.[16] In a former study, we have shown that even an *ex situ* rinsing by liquid carbon precursors on a Rh(111) surface results in well-ordered graphene layers provided that the decay of the precursor as well as the agglomeration of the remaining building blocks of carbon are controlled via an appropriate temperate ramping.[17] In case of Rh(111), this recipe results in the formation of a well-ordered $12 \times 12/11 \times 11$ superstructure that has been successfully used as a template for the buildup of hierarchical superstructures.[18]

In this study, we report on the epitaxial growth of graphene on a Ir/YSZ/Si(111) surface (here YSZ denotes a buffer layer of yttria-stabilized zirconium oxide) via the deposition of acetone, $(CH_3)_2CO$. It is shown that this route of synthesis also results in exactly one monolayer of graphene. Together with the results from our previous study concerning graphene formation on a Rh(111) surface,[17] the present results give strong evidence that (large-scale) graphene formation on transition metal surfaces by liquid carbon precursors represents a viable and easily controllable route that benefits from the lack of any apparative effort for carbon dosing.

II. EXPERIMENTAL

A. Experimental setup

The experiments were performed with a VG ESCA Mk II spectrometer that is described in detail in previous studies.[17,19–26] For photoelectron spectroscopy, Al-K_α

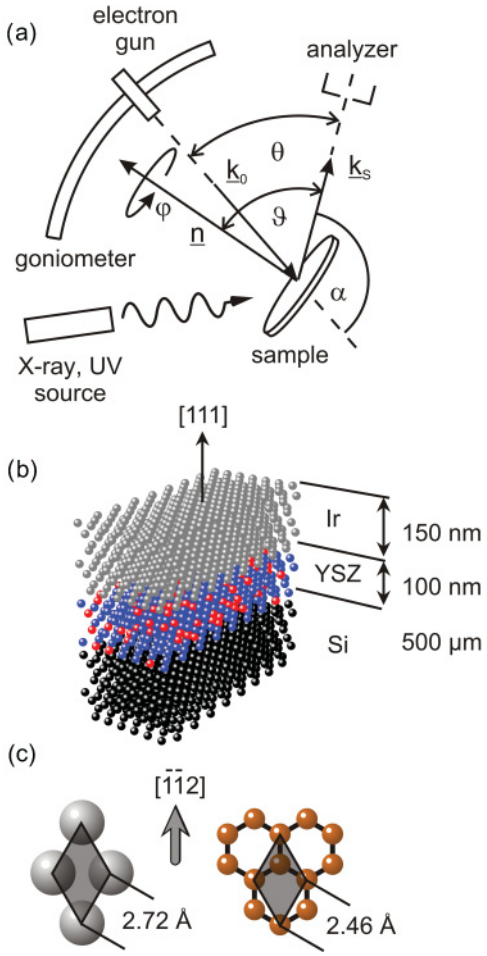

FIG. 1. (Color online) (a) Schematic drawing of the experimental setup. For angular resolved experiments, such as XPD, LEED, and FSM, the sample can be rotated by the polar angle ϑ and the azimuthal angle φ for mapping the whole 2π hemisphere above the surface of the sample by a fixed energy analyzer. (b) Schematic drawing of the Ir/YSZ/Si(111) multilayer substrates. (c) Unit cells of the Ir(111) topmost layer and of graphene.

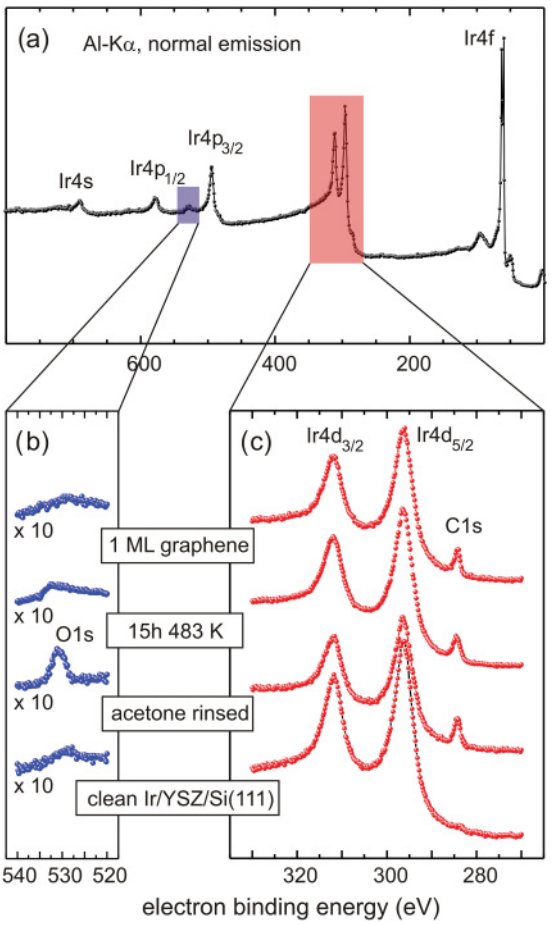

FIG. 2. (Color online) XPS data (Al-K_α, $\hbar\omega = 1486.6$ eV, normal emission $\vartheta = 0°$) for several stages of graphene formation on the Ir/YSZ/Si(111) substrate. (a) Survey spectrum, (b) O-1s spectra, and (c) C-1s spectra. (From bottom to top) Clean Ir surface, after deposition of acetone precursor, after first annealing for 15 h at 483 K, after several steps of annealing (cf. temperature ramping in Fig. 7) with final annealing at 978 K. Satellites from Ir-4$d_{5/2}$ (∼295 eV) by Al-$K_{\alpha 3}$ and Al-$K_{\alpha 4}$ contributions (due to non-monochromatic x rays) in the range of C-1s (∼284.5 eV) have been eliminated numerically by shifting/weighting the spectra by 9.8 eV/6.4% and 11.8 eV/3.2%, respectively, and subtracting them from the raw data. In case of the O-1s binding energy range, the intensities displayed in the spectra for the clean sample and after graphene formation represent rather contributions from the energy loss background (e.g., plasmons) of the Ir-4$p_{3/2}$ line than contributions from O-1s. In the survey spectra, the absence of oxygen was also cross-checked by the missing O-KVV Auger intensities.

radiation with $\hbar\omega = 1486.6$ eV (XPS) and He-I radiation with $\hbar\omega = 21.2$ eV (UPS) were used. For angle-resolved experiments, i.e., x-ray photoelectron diffraction (XPD), Fermi surface mapping (FSM), and low-energy electron diffraction (LEED), the whole 2π k space above the sample is probed by using a manipulator with two rotational degrees of freedom (polar angle ϑ and azimuthal angle φ). In contrast to commercial LEED systems, the reciprocal surface lattice is mapped by angular-resolved electron-energy-loss spectroscopy (AREELS). Here, the intensity of the elastically scattered electrons at $\Delta E = 0$ is recorded for varying the angular setting (ϑ, φ) by running the angular part and the spectroscopic part of the setup in the XPD and EELS mode (primary energy $E_0 = 45$ eV), respectively, i.e., $I(\Delta E = 0)$ is recorded for varying angular settings (ϑ, φ), cf. Fig. 1(a).

B. Ir/YSZ/Si(111) substrates

Epitaxial YSZ films on 4-in. Si(111) wafers were prepared by pulsed laser deposition (PLD) using a KrF excimer laser (pulse duration: 25 ns; pulse energy: 850 mJ) and a cylindrical ablation target.[27] For the fabrication of the target we used a mixture of Y_2O_3 and ZrO_2 powder (21.4 mol% $YO_{1.5}$) which was compressed at 1.5 kbar and then sintered for 25 h at 1773–1923 K. Ablation was done at a substrate temperature of 1023 K. To reduce the native oxide of the Si(111) substrate, the first 500–1000 pulses were performed in high vacuum. For the further growth the oxygen background pressure was increased to 5×10^{-4} mbar. The typical film thickness was 100 nm.

In the next step, 150-nm-thick iridium films were deposited on the oxide-buffered silicon by e-beam evaporation at 923 K.

The first 20 nm were grown with a low deposition rate of 0.004 nm/s. For the rest of the film a rate of 0.02 nm/s was applied.

Figure 1(b) schematically shows the stacking of the multilayer substrates. Figure 1(c) shows the unit cells of the hexagonal Ir(111) surface and graphene with the $[\bar{1}\bar{1}2]$ direction of the substrate and the armchair direction of graphene in real space referring to the symmetry axis of the first-order spots in reciprocal space.

C. Preparation of the graphene films

The preparation of epitaxial graphene on the Ir/YSZ/Si(111) multilayer substrates was similar to the procedure described in Refs. 17, 18. First, the samples are cleaned by cycles of Ar ion etching (3 kV, 1 μA/cm^2 for a few minutes) and annealing at 900–1000 K until no O-1s and C-1s intensities are detected in XPS and a sharp LEED pattern with nearly no background intensity is observed. In a second step, the clean surface of the sample is rinsed *ex situ* with acetone for a few seconds and transferred to UHV. After degassing for 12 h at room temperature, the samples were annealed by increasing the temperature stepwise up to 1000 K.

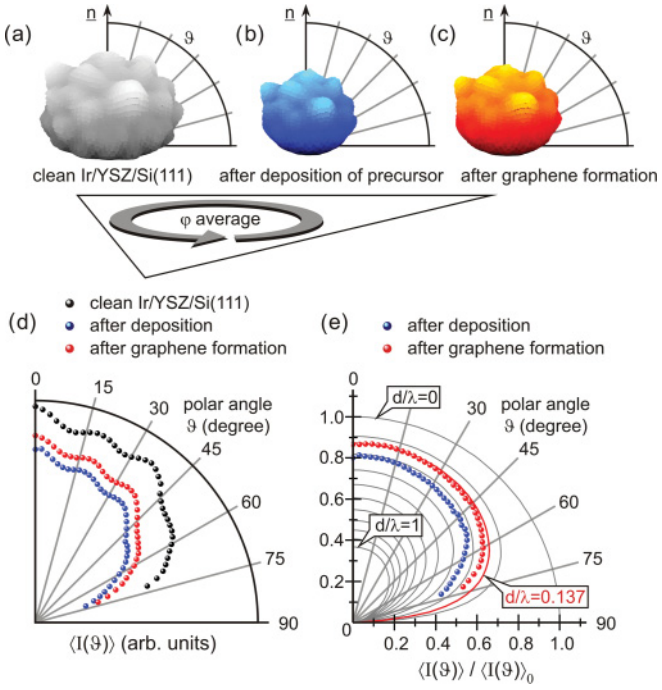

FIG. 3. (Color online) Estimation of the thickness of the carbon layer by attenuation of the Ir-4f photoelectron intensity in XPD. (a) Angular Ir-4f intensity distribution for clean Ir/YSZ/Si(111) substrate (Al-K$_\alpha$ radiation, $\hbar\omega = 1486.6$ eV); (b) same as (a) after deposition of acetone precursor; (c) same as (a) after graphene formation at 978 K; (d) azimuthally averaged Ir-4f polar intensity distribution $\langle I(\vartheta,d)\rangle$ for the clean Ir/YSZ/Si(111) surface (black, $\langle I(\vartheta)\rangle_0$), after deposition of acetone precursor (blue) and after graphene formation (red), as extracted from (a)–(c); (e) intensity ratio $\langle I(\vartheta,d)\rangle/\langle I(\vartheta)\rangle_0$ as extracted from (d) after deposition (blue) and after graphene formation (red). The gray solid lines represent the ratio $\sim\exp(-d/\lambda\cos\vartheta)$ for $d/\lambda = 0$ to $d/\lambda = 1$ (from outside to inside in steps of $d/\lambda = 0.1$). After graphene formation, the experimental data are very close to the red line that represents the intensity ratio for one monolayer graphene with $d/\lambda = 0.137$ for electron mean free path $\lambda = 2.44$ nm[30] and a monolayer thickness of $d = 0.335$ nm, as given by the interlayer spacing of graphite.

III. RESULTS AND DISCUSSION

A. Elemental composition of the surface by XPS

For the clean Ir/YSZ/Ir(111) sample, the XPS data in Fig. 2 exhibit intensities only from the Ir(111) surface without any significant signals from oxygen or carbon [cf. bottom row in Figs. 2(b)–2(c)]. After the *ex situ* deposition of the acetone precursor and degassing in UHV, distinct O-1s and C-1s signals are visible. In Figs. 2(b)–2(c), second row, the O-1s and C-1s intensities (as weighted with the cross sections by Yeh and Lindau)[28] provide a C:O = 3:0.85 ratio that is close to the 3:1 stoichiometry of the precursor [acetone = $(CH_3)_2CO$].

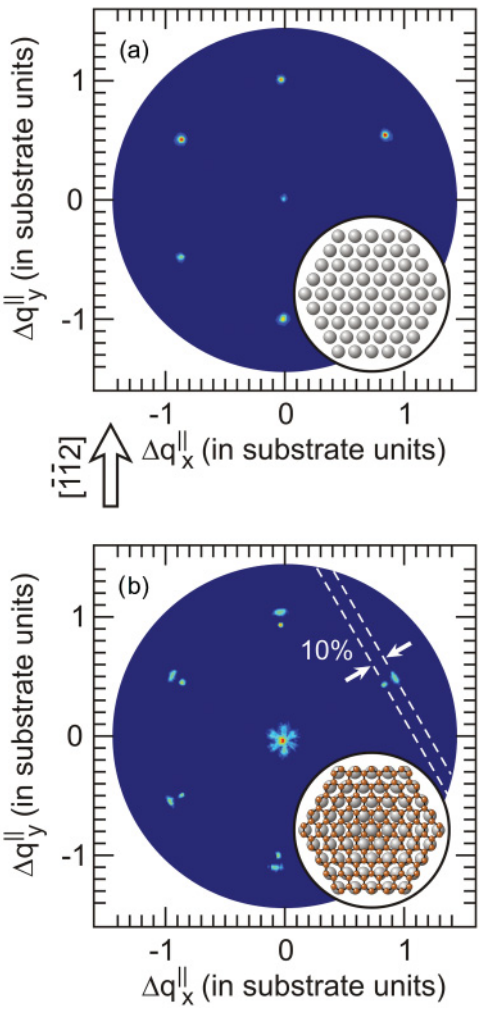

FIG. 4. (Color online) LEED patterns ($E_0 = 45$ eV) for (a) a clean Ir/YSZ/Si(111) surface and (b) after graphene formation. In (b), satellite spots just appear around the (0,0) spot. The weak satellite intensities around the (1,0) spots are not visible in this representation (see text).

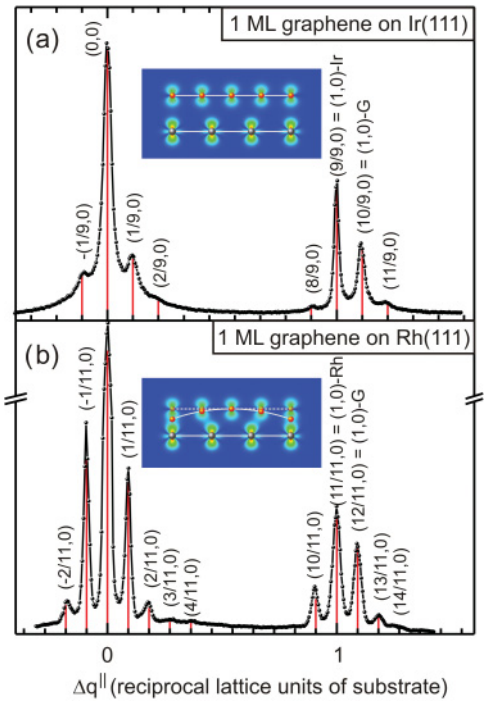

FIG. 5. (Color online) Polar intensity plots (LEED, $E_0 = 45$ eV) along the $[\bar{1}\bar{1}2]$ symmetry axis of the substrate for one monolayer graphene on (a) a weakly interacting Ir/YSZ/Si(111) surface and on (b) a strongly interacting Rh/YSZ/Si(111) surface from Ref. 17. Peaks are labeled in fractions of reciprocal lattice units according to the size of the supercell. Satellite intensities depend on the corrugation of the epitaxial layer (cf. Appendix). The insets schematically show for a linear 4/3 chain the local variation of orbital overlap for large and small interface spacing. For large distances, as in (a), variation of overlap is small, resulting in small corrugation and small satellite intensities, and vice versa in (b).

Therefore, it can be excluded that a distinct decay of the precursor starts at room temperature, at least on the Ir(111) surface. Although the conservation of the precursor-like C:O ratio after liquid precursor deposition was also observed for the growth of graphene on a Rh(111) surface (with acetone or acetaldehyde acting as precursors),[17] there is evidence that the onset of precursor decay depends on the catalytic properties of the particular substrate. On a Pt(111) surface, e.g., precursor decay starts immediately after deposition even at room temperature.[29]

After annealing at 483 K for a few hours, the O-1s intensity in Fig. 2(b), third row, has nearly dropped to the background values for the clean sample. Further annealing finally results in a complete vanishing of the O-1s signal. Thus, in spite of iridium's affinity to oxygen, apparently no stable oxide is formed during the decomposition of the acetone precursor. After annealing at 978 K, i.e., after the formation of single layer graphene (as derived from the XPD, LEED, and FSM data discussed below), the C-1s signal in Fig. 2(c), fourth row, displays nearly the same intensity as after deposition, indicating that during annealing nearly all the carbon that remains after degassing is finally transformed into graphene.

B. Thickness of the carbon layer by XPD

After final annealing at 978 K, the thickness of the carbon layer was determined by the attenuation of the Ir-4f photoelectron intensity in XPD. The angular intensity distribution of photoelectrons, as emitted from a crystalline target, is determined by the forward focusing due to the scattering from the atoms surrounding an emitting atom. The presence of an additional crystalline carbon layer can affect the angular intensity distribution from the substrate in two ways: In general, there is an attenuation by the new layer, but for particular directions, intensity from the substrate can also increase by additional forward focusing from the scattering at the atoms of the new layer. In order to reduce the latter effect, the Ir-4f intensity was recorded within the full hemisphere above the sample for several stages of graphene formation, cf. Figs. 3(a)–3(c). The mean polar intensity distribution was determined by averaging over all azimuthal directions for each polar angle, as depicted in Fig. 3(d). The thickness d of an epitaxial film can be estimated via the attenuated substrate intensity $\langle I(\vartheta)\rangle$ by the polar intensity ratio

$$\langle I(\vartheta)\rangle / \langle I(\vartheta)\rangle_0 = \exp\left(-\frac{d}{\lambda \cos\vartheta}\right),$$

with $\langle I(\vartheta)\rangle_0$ and λ describing the polar intensity distribution for the clean substrate (here Ir-4f) and the electron mean free path, respectively. In Fig. 3(e), the experimental intensity ratio after graphene formation at 978 K is compared to the calculated intensity ratios for one monolayer. Assuming that the thickness of single-layer graphene is represented by the interlayer spacing of graphite along the c axis ($d = 3.35$ Å) and that the electron mean free path for the graphene layer is similar to that of graphite ($\lambda = 24.4$ Å),[30] one gets $d/\lambda = 0.137$, as represented by the red curve in Fig. 3(e). Since the experimental data points are quite close to this curve, the estimation of the film thickness by XPD (together with the

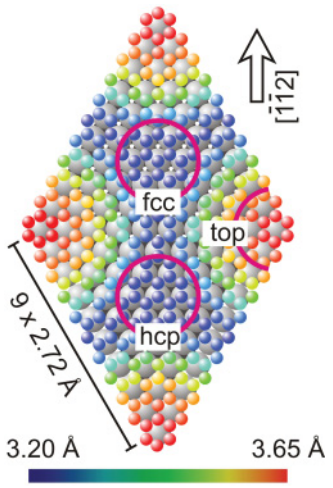

FIG. 6. (Color online) The surface structure of graphene on Ir(111) can be approximated by a commensurate 10 × 10/9 × 9 supercell with a corrugation of about 0.45 Å,[12] as caused by the enhanced bonding strength at fcc and hcp sites and the reduced bonding strength at top sites [note that the terms "fcc," "hcp," and "top," (cf. red circles), refer to the positions of the centers of the honeycomb, not to the positions of the carbon atoms].

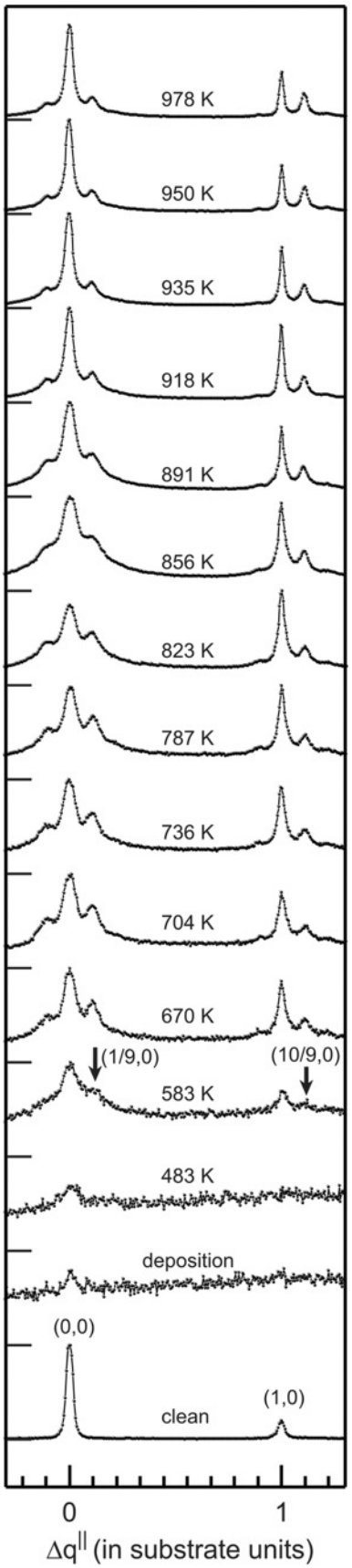

FIG. 7. Temperature-dependent LEED profiles ($E_0 = 45$ eV) along the $[\bar{1}\bar{1}2]$ direction. The first graphene-related intensities are observed at 583 K. For details, see text.

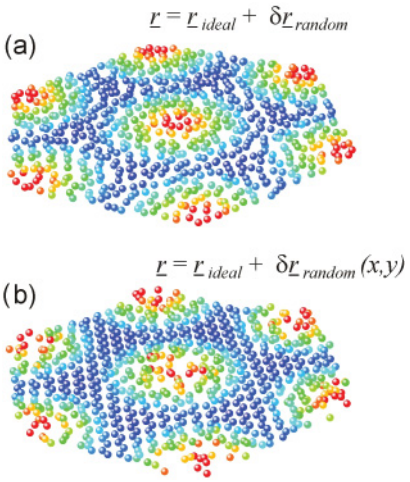

FIG. 8. (Color online) Schematic representation of the growth models for graphene on Ir(111). In (a), disorder is uniformly distributed throughout the supercell. The displacement of the carbon atoms from the positions of the ideal corrugated graphene layer[12] is described by a displacement amplitude $|\delta\underline{r}|$ that is weighted with a random number in the range $(-1 \ldots 1)$. The displacement amplitude does not depend on the position within the supercell. In (b), the displacement amplitude depends on the position within the supercell, i.e., $|\delta\underline{r}(x,y)|$, and decreases when going from the less stable top sites to the stable fcc or hcp sites. In both cases, the displacement amplitudes decrease with increasing order (i.e., increasing temperature in experiment) and drop to zero for the perfectly ordered graphene layer with a corrugation according to Ref. 12.

data discussed below) gives strong evidence for the formation of single-layer graphene.

C. Surface structure by LEED

For the clean Ir(111) surface the LEED data in Fig. 4(a) display a sharp hexagon of threefold symmetry due to the fcc stacking along the [111] axis. After the formation of a monolayer graphene, the LEED pattern in Fig. 4(b) just exhibits a second hexagon that is expanded by about 10%, according to the 10.5% lattice mismatch [2.72 Å for Ir(111) surface lattice vs. 2.46 Å for graphene]. In addition, the (0,0) spot is surrounded by a hexagonal halolike intensity distribution, but, in contrast to epitaxial graphene on other surfaces, such as Rh(111),[15,17,31] Ru(0001),[31–34] or SiC(0001),[5] this halolike structure, which is assigned to the formation of a $n \times n/m \times m$ Moiré pattern, is not observed around the (1,0) spots. However, when inspected in detail, the polar intensity plot along the $[\bar{1}\bar{1}2]$ symmetry axis in Fig. 5(a) also exhibits very weak satellite contributions around the (1,0) spots.

In terms of the strength of the satellite spots, the present LEED data are similar but not in full accordance to those observed for epitaxial graphene on Ir(111) by CVD of ethylene[35] or propene.[31] In both studies, the satellite spots are clearly visible, even around the Ir (1,0) spots, but compared to other substrates, such as Rh(111), they appear less distinct.[31] However, since these LEED patterns were recorded at different primary energies (60 eV in Ref. 31, 80.4 eV in Ref. 35, 45 eV in the present study) it is difficult to compare intensity distributions without taking I-V effects and apparatus specific

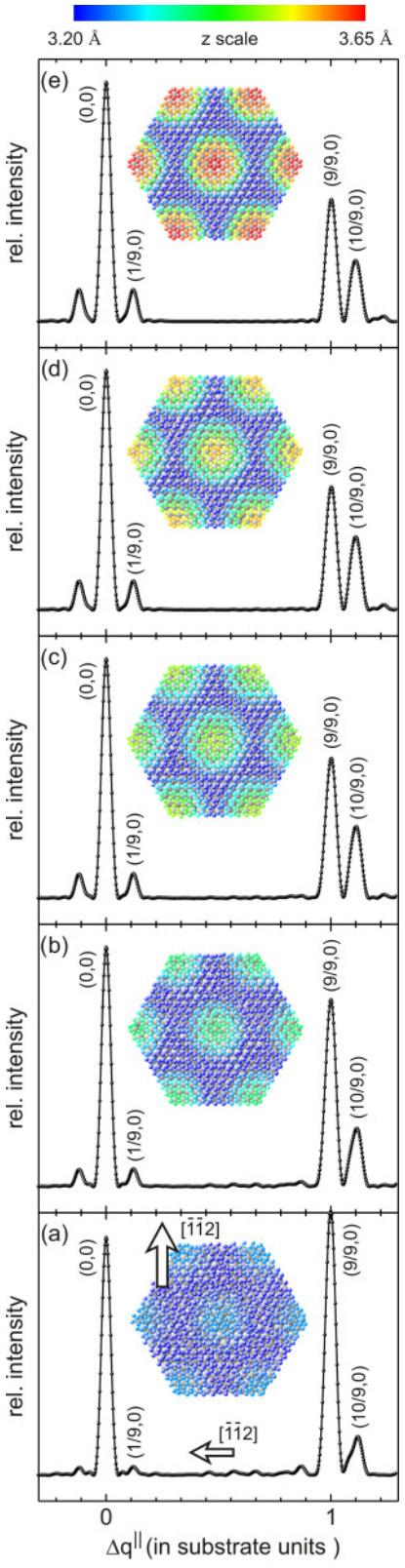

FIG. 9. (Color online) Simulation of LEED profiles along $[\bar{1}\bar{1}2]$ for different stages of order according to the growth model from Fig. 8(a) with disorder distributed uniformly throughout the supercell. With increasing order (i.e., temperature) the displacement amplitude decreases from (a)–(e). The surface models also represent the finite clusters with which the simulation was calculated. Intensities are normalized to (0,0) intensity.

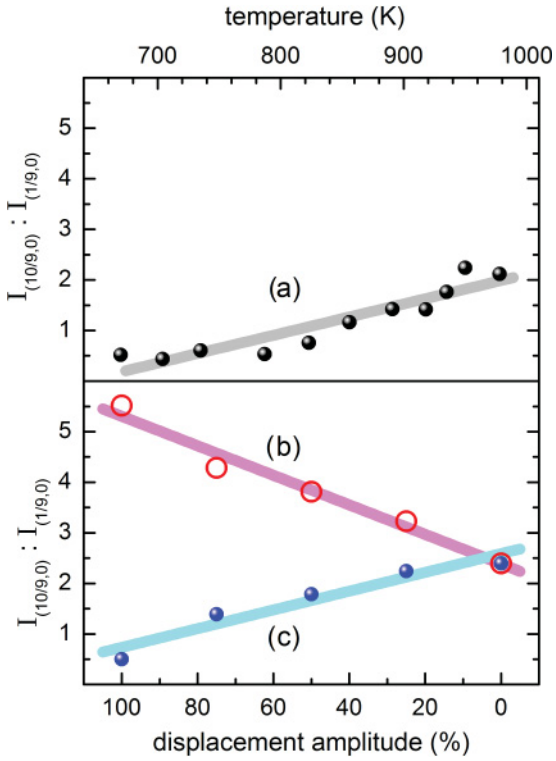

FIG. 10. (Color online) Intensity ratios $I_{(10/9,0)} : I_{(1/9,0)}$ from (a) the experimental LEED data (Fig. 7) and from the LEED simulations for (b) homogeneous ordering (Fig. 9) and for (c) backbonelike ordering (Fig. 11). The experimental intensity ratios in (a) follow the data in (c) rather than the data in (b).

parameters into account. In Fig. 5(b), we therefore refer to the LEED data for epitaxial graphene on a similar Rh/YSZ/Si(111) substrate with the graphene monolayer being prepared by the same recipe and probed by the same experimental setup with the same primary energy.[17] Compared to graphene on the weakly interacting (see below) Ir(111) surface, the contributions from the satellite spots are much more enhanced for graphene on the strongly interacting Rh(111) surface.

What is the main reason for the appearance of such satellite spots (that are also observed for epitaxial monolayers of boron nitride[24,36,37]) in a LEED experiment? The lattice mismatch of graphene and the surface of a particular substrate results in a spatial variation of the local atomic configuration throughout the $m \times m/n \times n$ supercell [$m \sim 10$, $n = 9$ for graphene on Ir(111); see Fig. 6]. Depending on the position within the supercell, the centers of the honeycombs are placed on top, on fcc or hcp sites of the substrate (cf. circles in Fig. 6), or in between, resulting in a spatial variation of the interaction between the carbon atoms and the atoms of the substrate, with the overall degree of interaction depending on the distance between graphene and the substrate surface. Therefore, a spatial modulation of electron density (as represented by the scattering factors in a LEED experiment) as well as corrugation may occur, both leading to different weights with which the partial waves that are scattered from the epitaxial layer contribute to the interference pattern.

According to LEED simulations (see Appendix), satellite intensities are much more sensitive to corrugation than to

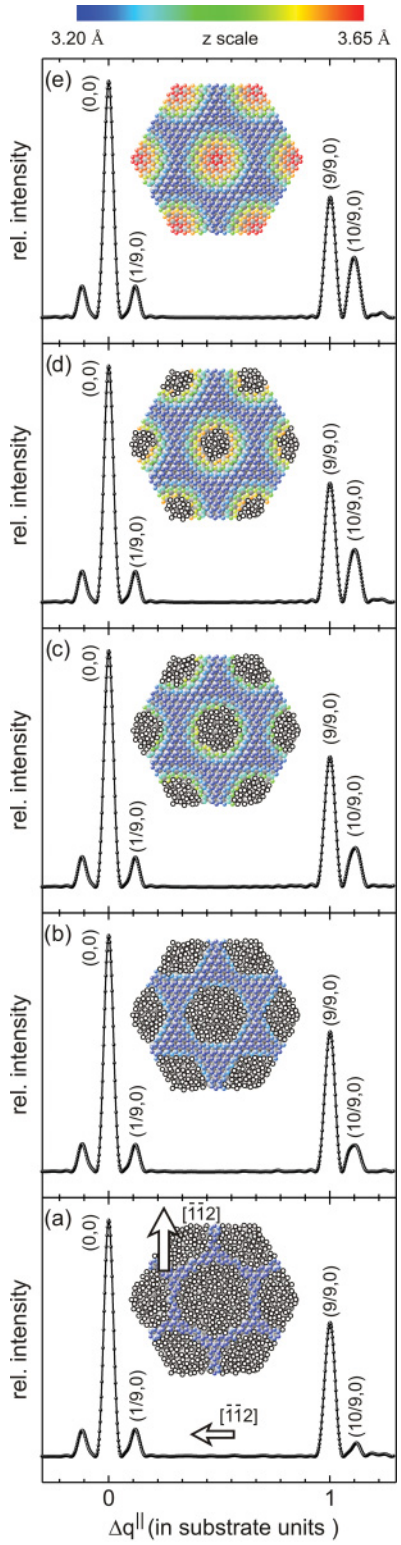

FIG. 11. (Color online) Simulation of LEED profiles along [$\bar{1}\bar{1}$2] for different stages of order according to the growth model from Fig. 8(b) with disorder depending on the position within the supercell. Ordering starts with a narrow network along the fcc and hcp sites, as in (a), and with increasing order or temperature, [(b)–(e)], this network is expanded over the whole supercell. Here, disordered areas are represented by white circles. The surface models also represent the finite clusters with which the simulation was calculated. Intensities are normalized to (0,0) intensity.

modulations of the scattering factors. Therefore, the satellite spots that are often assigned to the presence of a Moiré pattern in literature do not represent a Moiré pattern just in terms of a coincidence lattice by the superposition of two lattices. They rather represent the interaction throughout the Moiré pattern in terms of corrugation (it is worth noting that the LEED simulations for commensurate and incommensurate lattices exhibit only marginal differences that would be hardly detectable by a usual LEED setup). Therefore, the different satellite intensities in Fig. 5 predict the corrugation to be much larger for graphene on Rh(111) than for graphene on Ir(111). This LEED-based assumption of small corrugation for graphene on Ir(111) is supported by the study of Preobrajenski *et al.*[31] where for the series Pt(111), Ir(111), Rh(111), Ru(0001) an increasing degree of corrugation for graphene is derived from the C-1s NEXAFS and C-1s photoelectron spectra. The same tendency for corrugation is confirmed also by other studies using complementary methods. The small corrugation of graphene on the weakly interacting Ir(111) surface is further supported experimentally by STM, 0.2–0.3 Å,[38] and theoretically by DFT calculations, 0.27 Å[11]–0.45 Å.[12] For graphene on the strongly interacting Ru(0001) surface, a larger corrugation of 1 Å is found by STM[39] which is also in the same range as the calculated value of about 1.5 Å.[10,33] Similarly, the corrugation for graphene on Rh(111) was found to be up to 1.5 Å in STM.[40]

For epitaxial graphene on TM surfaces the bonding strength decreases from the 3*d* to the 5*d* row and it also decreases within one row with increasing number of *d* electrons,[16] resulting in an enhanced equilibrium distance between graphene and the metal surface for weak bonding systems, as predicted by van der Waals density-functional theory.[41] A similar behavior was also predicted for epitaxial layers of boron nitride on TM surfaces[42,43] (although for BN, one has to consider the competing interactions of the TM surface with two different sublattices). As a rule of thumb, the smaller the (mean) distance between graphene and the substrate, the larger the corrugation since covalent bonding by the overlap of the d_z^2 orbitals of the substrate and the p_z orbitals of the carbon atoms strongly varies throughout the supercell, as schematically sketched in the insets in Fig. 5 (for a quantitative description of this phenomenon, cf. Ref. 12).

D. Growth mode of graphene formation

The onset of graphene formation and growth kinetics for graphene on Ir(111) have been investigated by temperature dependent LEED experiments, as shown in Fig. 7. Compared to the clean Ir(111) surface, the polar intensity profiles along [$\bar{1}\bar{1}$2] after deposition at room temperature and after first annealing at 483 K just exhibit only weak specular (0,0) spots on large background intensities, indicating a strongly disordered surface. At further annealing, graphene formation starts quite early in the range of 583 K, as indicated by the appearance of the (1,0) principal spot of graphene (i.e., the (10/9, 0) spot in terms of the superstructure) and the (1/9, 0) satellite spot (black arrows). With increasing temperature, the disordered fragments from precursor decay (probably :C = C: units according to Ref. 17) agglomerate to increasing graphene domains as indicated by the increased peak-to-background

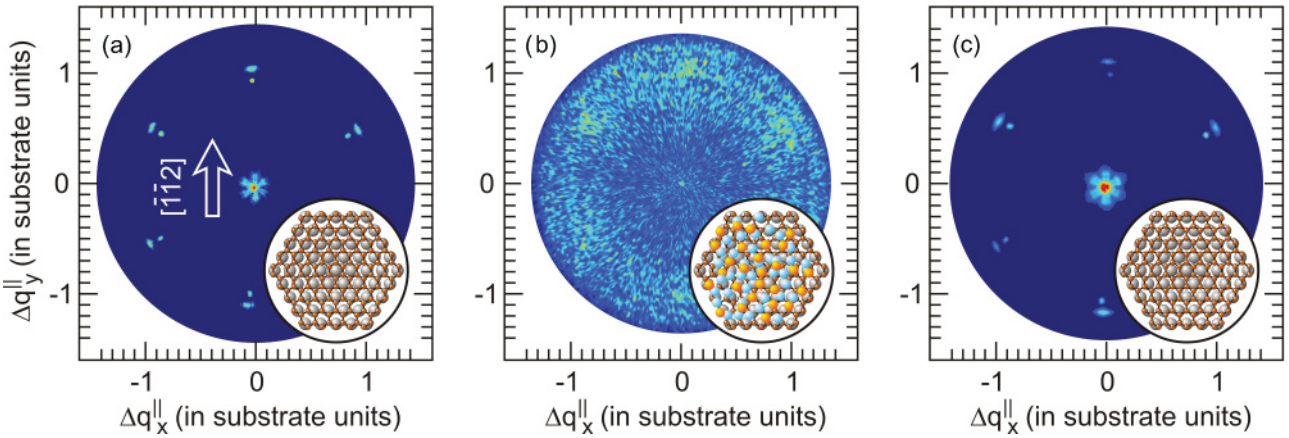

FIG. 12. (Color online) LEED pattern of (a) an *in situ* prepared (978 K) monolayer of graphene on Ir(111), (b) after storage for several weeks under ambient conditions (with diffuse LEED spots still visible), and (c) after regeneration in UHV by annealing at 973 K for several hours.

ratios and the smaller peak widths. In principle, the LEED profile after annealing at 670 K exhibits all characteristics (with different degree of order) as the profile after final annealing at 978 K, i.e., after formation of a well-ordered graphene monolayer. The most prominent feature in the temperature series in Fig. 7 concerns the relative intensity variations of the graphene-related (1/9,0) and the (10/9,0) spots. At 670 K, i.e., after the onset of graphene formation, the intensity of the (1/9,0) superstructure spot is larger than the intensity of the (10/9,0) spot but with increasing temperature (i.e., with increasing order), the intensity ratio of both spots then becomes reversed.

In order to assign this behavior to a particular growth mode, LEED simulations have been performed for two different scenarios. In both cases, disorder is described by a random displacement of the carbon atoms out of the positions for an ideal corrugated graphene monolayer with the amplitude of displacement decreasing with increasing order. In the first case, disorder is distributed homogeneously throughout the supercell, i.e., the displacement amplitude does not depend on the position of a carbon atom within the supercell, cf. Fig. 8(a). In the second case, disorder is distributed not homogeneously with the displacement amplitude depending on the position of a particular carbon atom within the supercell. Here, displacement correlates with the distance from the stable hcp and fcc configuration sites, i.e., random displacement increases while approaching the less stable on-top configuration sites. The second scenario therefore describes a kind of backbone growth by forming a network of increased order along the hcp and fcc sites, cf. Fig. 8(b). For both growth models, the corrugation of the ideal graphene monolayer (zero displacement for all carbon atoms) is given by the values proposed by the recent vdW-DFT results of Busse *et al.*,[12] i.e., $z = 3.20$ Å for hcp and fcc configuration and $z = 3.65$ Å for on-top configuration.

Figure 9 shows the simulations of LEED profiles along the [$\bar{1}\bar{1}$2] direction for the case of homogeneous disorder according to Fig. 8(a). The degree of order increases from Figs. 9(a) to 9(e), as depicted by the corresponding clusters that also represent the lattice input for simulation. Apart from the missing background intensities (that cannot be simulated in an appropriate way for such small clusters), the simulations are not in accordance with the experimental data in Fig. 7 in terms of the intensity ratio $I_{(10/9,0)}$:$I_{(1/9,0)}$. If (dis-)order of the carbon atoms is distributed homogeneously, this intensity ratio decreases with increasing order [cf. Fig. 10(b)], in contrast to the experimental intensity ratio from Fig. 7 that exhibits the reversed temperature (i.e., order) dependence in Fig. 10(a).

Figure 11 shows LEED simulations according to the growth model from Fig. 8(b), starting with the nucleation of narrow ribbons connecting the hcp and fcc configuration sites. With increasing order, these ribbons become extended and finally cover the whole supercell. For this growth model, the $I_{(10/9,0)} : I_{(1/9,0)}$ intensity ratio in Fig. 10(c) increases with increasing order similar to the temperature dependence of the experimental intensity ratio in Fig. 10(a).

According to these results, it can be assumed that the growth of graphene on Ir(111) takes place via a nucleation at the most stable configuration sites for which the number of carbon atoms being on top of the substrate atoms is largest.

E. Stability of the graphene layers

The stability of the graphene monolayer, as derived after final annealing at 978 K, was tested in terms of reactivity under ambient conditions by an *ex situ* storage of the sample on a laboratory bench for several weeks. Compared to the LEED pattern in Fig. 12(a) for freshly prepared graphene, *ex situ* storage leads to diffuse LEED pattern in Fig. 12(b) but with the hexagonal scattering anisotropy still present. Since annealing in UHV at 973 K restores the LEED pattern of the graphene monolayer in Fig. 12(c), it is obvious that *ex situ* storage just results in additional layers of physisorbed species that can be simply degassed by appropriate temperatures in UHV.

F. Electronic structure by FSM

In contrast to free-standing graphene, the electronic properties of epitaxial graphene on TM surfaces can be affected by the interaction with the substrate, leading to a *p*-type or *n*-type doping with the Fermi energy being shifted below or

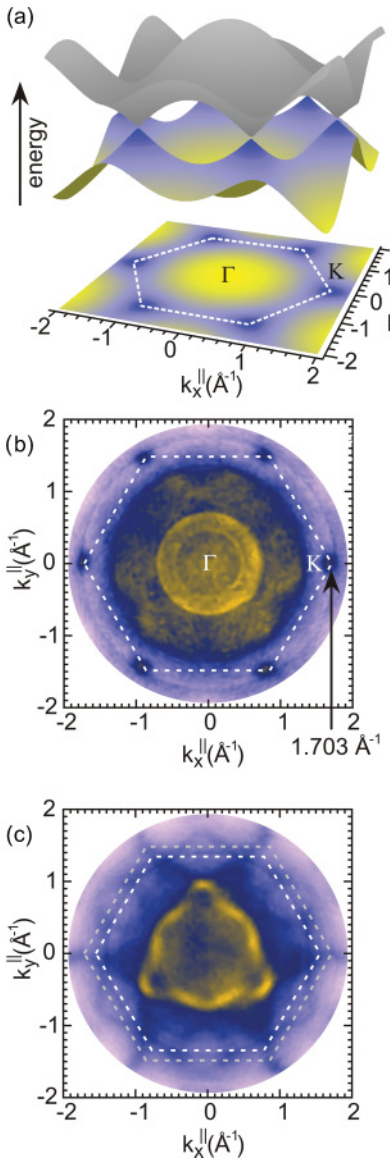

FIG. 13. (Color online) (a) Band structure of graphene as derived from the most simple tight-binding ansatz[1] with the Dirac cones meeting at the *K* points of the Brillouin zone; (b) Fermi surface mapping (He I radiation) for one monolayer graphene on Ir(111) with distinct intensities at $k^{\parallel} \sim 1.7$ Å^{-1} at the corners of the Brillouin zone [cf. *K* points in (a) are at $4\pi/3a = 1.703$ Å^{-1} for $a = 2.46$ Å]; (c) Fermi surface mapping of the clean Ir/YSZ/Si(111) surface as a reference. The smaller hexagon corresponds to the surface Brillouin zone of the substrate.

above the Dirac point, respectively.[41] However, due to the predictions of small corrugation at large overall distances for graphene on Ir(111)[11,12] it can be expected that the electronic properties of such a weakly interacting graphene layer are close to those of free-standing two dimensional graphene. Indeed, the band structure of graphene on Ir(111), as prepared by CVD of ethene, remains nearly unchanged according to the ARUPS data by Pletikosic *et al.*[44] with the Fermi energy slightly shifting about 100 meV below the Dirac point.

For epitaxial graphene on Ir(111) by liquid precursor deposition of acetone, a similar behavior is observed. In Fig. 13, the band structure of graphene, as derived in first-order approximation in the tight-binding ansatz by Wallace,[1] is compared to the Fermi surface mapping (FSM, $\hbar\omega = 21.22$ eV by He-I radiation) for the clean Ir(111) surface and after formation of a graphene monolayer. In contrast to the part of the 3D Fermi surface that is probed by the particular photon energy for clean Ir(111) in Fig. 13(c), the FSM data in Fig. 13(b) for one monolayer graphene on Ir(111) exhibit six additional spots. These spots appear exactly at the *K* points of the Brillouin zone of graphene at $4\pi/3a = 1.703$ Å^{-1}. Due to the poor energy resolution of about 200 meV used in this experiment, it is not possible to determine the exact position of the Dirac cone with respect to the Fermi energy. However, the appearance of distinct intensities at the *K* points rather confirm than contradict the presence of one monolayer graphene on Ir(111), as derived from the LEED and XPD data.

IV. SUMMARY

During the past few years, the literature has reported on a large variety of experimental studies on the epitaxial growth of graphene on Ir(111) revealing a weak interaction between the Ir(111) surface and the graphene lattice so the latter can be considered as quasi-free-standing graphene.[11,12,31,35,38,44] All of these studies have in common that carbon is provided via CVD of gaseous precursors that are decomposed at high temperatures in the range of 1000 K or above.

In the present study, it is shown that the method of liquid phase deposition that had turned out to be successful for epitaxial growth of graphene on Rh(111)[17,18] is also a viable alternative method to grow epitaxial graphene monolayers on Ir(111). Although carbon is provided in the most simple and rather uncontrolled way, the observation of an ordered graphene monolayer after an appropriate temperature ramping clearly indicates that the self-assembly mechanism represents the crucial factor in the graphene formation process. The temperature-dependent experiments show that immediately after the completion of the precursor decay the formation of graphene starts at quite low temperatures of about 600 K. For the transformation to well-ordered graphene monolayers an increase of the temperature to about 1000 K is required. We suppose that self-assembly takes place via a backbonelike growth mechanism along the hcp and fcc sites of the supercell since nucleation at these sites is favored due to the largest (but compared to other TM surfaces still small) interaction. First, this growth mechanism derived from experimental data in reciprocal space should be confirmed by real space data, i.e., STM experiments. Moreover, it suggests growth of networks of graphene nanoribbons of tuneable width, as, e.g., by temperature-dependent selective desorption of the weaker bonded disordered carbon species.

ACKNOWLEDGMENTS

This work was supported by the framework program "Materials Innovations for Industry and Society—WING" of the German Federal Ministry of Education and Research (Project No. 03×0107B) within the project "TIGeR: Tribological Innovation with Graphene: Extreme Reduction of Friction." M.S. and S.G. acknowledge support of this work by

the German Research Foundation (DFG) in the framework of the Priority Program 1459 "Graphene."

APPENDIX

The objective of our LEED simulations is to assign tendencies of the experimental data to a particular surface structure than to achieve a 1:1 correspondence between the experimental data and simulation by using a large variety of parameters. Therefore, we restrict our approach to the most simple, i.e., kinematic, ansatz, in which the diffraction pattern as resulting from the single scattering from a crystalline target represents the superposition of the scattered waves via[45]

$$I(\vartheta,\phi) \propto \left| \sum_{\text{Cluster}} f_j e^{i\Delta\underline{q}\underline{R}_j} \right|^2 = \left| \sum_{\text{Cluster}} f_j e^{i\Delta\underline{q}^{\parallel}\underline{R}_j^{\parallel}} e^{i\Delta\underline{q}^{\perp}\underline{R}_j^{\perp}} \right|^2 \tag{A1}$$

with $\Delta\underline{q} = \underline{k}_s - \underline{k}_0$ being the transfer of momentum, $\underline{k}_0$ and $\underline{k}_s$ being the wave vectors of the primary and scattered electron beam, respectively ($k_0(\text{Å}^{-1}) = k_s(\text{Å}^{-1}) = 0.512\sqrt{E_0(\text{eV})}$ for elastic scattering). Apart from the scattering factors [for which no k dependence is assumed, i.e., $f_j(\underline{k}_0,\underline{k}_s) \equiv f_j$], the LEED pattern is then determined only by the geometry of the applied lattice clusters within this approximation.

In the simplest case, the interface just consists of the topmost layer of the substrate at $z = 0$ and a flat epitaxial layer at $z = z_0$:

$$I(\vartheta,\phi) \propto \left| F \sum_{\text{substrate}} e^{i\Delta\underline{q}^{\parallel}\underline{R}_j^{\parallel}} + f e^{i\Delta q^{\perp} z_0} \sum_{\text{layer}} e^{i\Delta\underline{q}^{\parallel}\underline{R}_j^{\parallel}} \right|^2. \tag{A2}$$

The spatial modulation of the layer-substrate interaction throughout an $m \times m/n \times n$ supercell (or a $\sim m \times \sim m/n \times n$ Moiré period), as caused by the variation of local atomic configuration, can have a double impact.

First, there may be a spatial variation of electron density that is displayed by a modulation of the scattering factors. For a linear chain along the x direction (as discussed below), the scattering factors are then given by, e.g., a cosine-like modulation with the period $x_0 = n \cdot a_{\text{substrate}}$

$$f(x_j) = f_0 + \Delta f(x_j) = f_0 + \Delta f \cos\left(\frac{2\pi x_j}{x_0}\right).$$

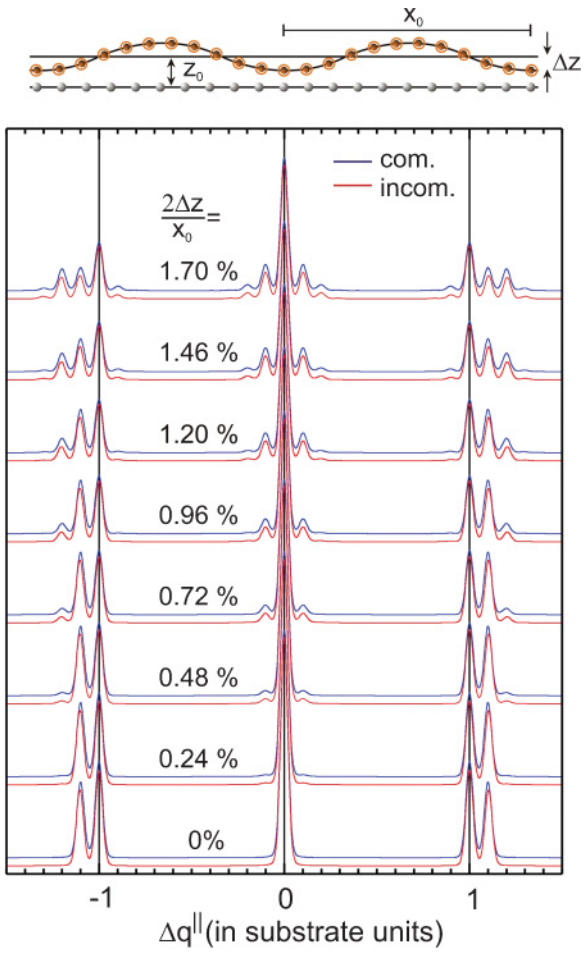

FIG. 14. (Color online) LEED simulation for a linear chain with a commensurate (blue) and an incommensurate (red) epitaxial layer for different corrugations. In the model structure, the full dots and open circles in the corrugated layer represent the positions for the commensurate and incommensurate case, respectively.

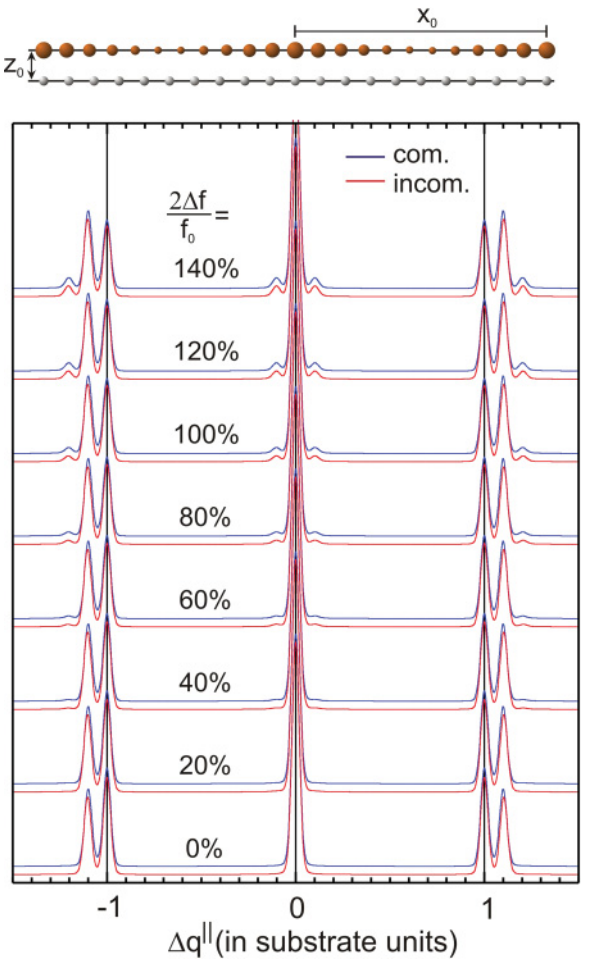

FIG. 15. (Color online) LEED simulation for a linear chain with a commensurate (blue) and an incommensurate (red) flat epitaxial layer for spatial variation of the scattering factors, as represented by the size of the atoms in the model structure.

For simplicity, only a modulation of the scattering factors of the atoms within the epitaxial layer is considered (taking also the substrate into account would not change the results). For a linear chain with f modulation but no corrugation of the layer, Eq. (A2) then reads:

$$I(\vartheta,\phi) \propto \left| F \sum_{\text{substrate}} e^{i\Delta q_x x_j} + e^{i\Delta q_z z_0} \times \sum_{\text{layer}} [f + \Delta f(x_j)] e^{i\Delta q_x x_j} \right|^2 . \quad \text{(A3)}$$

Second, the spatial modulation of the layer-substrate interaction can also cause a variation of the z positions for the atoms of the epitaxial layer, as, e.g.,

$$z_j(x_j) = z_0 + \Delta z(x_j) = z_0 + \Delta z \cos\left(\frac{2\pi x_j}{x_0}\right).$$

For a corrugation of the layer but constant scattering factors f, Eq. (A2) then reads:

$$I(\vartheta,\phi) \propto \left| F \sum_{\text{substrate}} e^{i\Delta q_x x_j} + f e^{i\Delta q_z z_0} \sum_{\text{layer}} e^{i\Delta q_x x_j} e^{i\Delta q_z \Delta z(x_j)} \right|^2 . \quad \text{(A4)}$$

In order to reveal the impact of modulations of both, i.e., scattering factors and corrugation, LEED profiles as calculated by Eqs. (A3) and (A4) are compared for a model system that consists of a linear chain of 80 substrate periods and an epitaxial layer forming a commensurate $m/n = 11/10$ superstructure or an incommensurate $m/n = 11.032\ldots/10$ Moiré pattern. For both cases, corrugation is varied at fixed scattering factors, Eq. (A4) and, conversely, Eq. (A3). Since 80 periods result in nearly δ-like peaks, the calculated LEED profiles are additionally convoluted with a Gaussian response function of about 0.1 Å^{-1} (comparable to the angular resolution in the experiment).

Figure 14 shows the calculated LEED profiles for the corrugation $2\Delta z/x_0$ (with $x_0 = 10a_{\text{substrate}}$) increasing from 0 to 1.70%. For no corrugation (0%), the LEED profile corresponds to a superposition of two separate lattices while for increasing corrugation the satellite intensities increase systematically until they become comparable to the principal spot intensities of the substrate and the epitaxial layer (e.g., at 1.70%). For each corrugation, there are only marginal differences between the commensurate and the incommensurate case. In a usual LEED setup these differences are hard to observe.

In Fig. 15 the scattering factors for a flat epitaxial layer are varied from 0 to 140%. Even for large variations of the scattering factors the satellite spots exhibit only weak intensities. Again, there are nearly no differences between the commensurate and incommensurate growth.

From Figs. 14 and 15 it is evident that even small corrugations have a much stronger impact on the appearance of satellite intensities than large modulations of the scattering factors (as representing spatial variation of electron density). For example, the strong 140% modulation of the scattering factors in Fig. 15 results in nearly the same weak satellite intensities as the small 0.8% corrugation in Fig. 14.

The LEED profiles in Figs. 9 and 11 have been calculated by expanding Eq. (A4) for a three-dimensional cluster with the cosinelike corrugation being replaced by a Gaussian-like corrugation that approaches the values by Busse *et al.*[12] for perfect order.

*Corresponding author: f.mueller@mx.uni-saarland.de

[1] P. R. Wallace, Phys. Rev. **71**, 622 (1947).
[2] A. K. Geim and K. S. Novoselov, Nat. Mater. **6**, 183 (2007).
[3] K. S. Novoselov, A. K. Geim, S. V. Morozov, D. Jiang, Y. Zhang, S. V. Dubonos, I. V. Grigorieva, and A. A. Firsov, Science **306**, 666 (2004).
[4] C. Stampfer, E. Schurtenberger, F. Molitor, J. Güttinger, T. Ihn, and K. Ensslin, Nano Lett. **8**, 2378 (2008).
[5] K. V. Emtsev *et al.*, Nat. Mater. **8**, 203 (2009).
[6] T. Filleter, J. L. McChesney, A. Bostwick, E. Rotenberg, K. V. Emtsev, Th. Seyller, K. Horn, and R. Bennewitz, Phys. Rev. Lett. **102**, 086102 (2009).
[7] C. Lee, Q. Li, W. Kalb, X. Z. Liu, H. Berger, R. W. Carpick, and J. Hone, Science **328**, 76 (2010).
[8] M. Müser and D. Shakhvorostov, Science **328**, 52 (2010).
[9] M. Dienwiebel, G. S. Verhoeven, N. Pradeep, J. W. M. Frenken, J. A. Heimberg, and H. W. Zandbergen, Phys. Rev. Lett. **92**, 126101 (2004).
[10] T. Brugger, S. Günther, B. Wang, J. H. Dil, M. L. Bocquet, J. Osterwalder, J. Wintterlin, and T. Greber, Phys. Rev. B **79**, 045407 (2009).
[11] A. T. N'Diaye, S. Bleikamp, P. J. Feibelman, and Th. Michely, Phys. Rev. Lett. **97**, 215501 (2006).
[12] C. Busse *et al.*, Phys. Rev. Lett. **107**, 036101 (2011).
[13] G. Nandamuri, S. Roumimov, and R. Solanki, Nanotechnology **21**, 145604 (2010).
[14] H. Ueta, M. Saida, C. Nakai, Y. Yamada, M. Sasaki, and S. Yamamoto, Surf. Sci. **560**, 183 (2004).
[15] P. W. Sutter, J. I. Flege, and E. A. Sutter, Nat. Mater. **7**, 406 (2008).
[16] J. Wintterlin and M. L. Bocquet, Surf. Sci. **603**, 1841 (2009).
[17] F. Müller *et al.*, Small **5**, 2291 (2009).
[18] A.J. Pollard *et al.*, Angew. Chem. **122**, 1838 (2010).
[19] F. Müller, R. de Masi, D. Reinicke, P. Steiner, S. Hüfner, and K. Stöwe, Surf. Sci. **520**, 158 (2002).
[20] F. Müller, P. Steiner, Th. Straub, D. Reinicke, S. Palm, R. de Masi, and S. Hüfner, Surf. Sci. **442**, 485 (1999).
[21] F. Müller, R. de Masi, P. Steiner, D. Reinicke, M. Stadtfeld, and S. Hüfner, Surf. Sci. **459**, 161 (2000).
[22] F. Müller, K. Stöwe, and H. Sachdev, Chem. Mater. **17**, 3464 (2005).
[23] F. Müller, S. Hüfner, and H. Sachdev, Surf. Sci. **602**, 3467 (2008).
[24] F. Müller, S. Hüfner, and H. Sachdev, Surf. Sci. **603**, 425 (2009).
[25] R. de Masi, D. Reinicke, F. Müller, P. Steiner, and S. Hüfner, Surf. Sci. **515**, 523 (2002).
[26] R. de Masi, D. Reinicke, F. Müller, P. Steiner, and S. Hüfner, Surf. Sci. **516**, L515 (2002).
[27] S. Gsell, M. Fischer, M. Schreck, and B. Stritzker, J. Cryst. Growth **311**, 3731 (2009).

[28]J. J. Yeh and I. Lindau, At. Data Nucl. Data Tables **32**, 1 (1985).
[29]S. Grandthyll, S. Hüfner, and F. Müller, unpuplished data.
[30]B. Lesiak, A. Jablonski, Z. Prussak, and P. Mrozek, Surf. Sci. **223**, 213 (1989).
[31]A. B. Preobrajenski, May Ling Ng, A. S. Vinogradov, and N. Mårtensson, Phys. Rev. B **78**, 073401 (2008).
[32]W. Moritz, B. Wang, M.-L. Bocquet, T. Brugger, T. Greber, J. Wintterlin, and S. Günther, Phys. Rev. Lett. **104**, 136102 (2010).
[33]D. Martoccia *et al.*, Phys. Rev. Lett. **101**, 126102 (2008).
[34]S. Marchini, S. Günther, and J. Wintterlin, Phys. Rev. B **76**, 075429 (2007).
[35]A. T. N'Diaye, J. Coraux, T. N. Plasa, C. Busse, and T. Michely, New J. Phys. **10**, 043033 (2008).
[36]F. Müller, H. Sachdev, S. Hüfner, S. Gsell, and M. Schreck, Phys. Rev. B **82**, 075405 (2010).
[37]M. Corso, W. Auwärter, M. Muntwiler, A. Tamai, T. Greber, and J. Osterwalder, Science **303**, 217 (2004).
[38]S. Barja, M. Garnica, J. J. Hinarejos, A. L. Vázquez de Parga, N. Martín, and R. Miranda, Chem. Commun. **46**, 8198 (2010).
[39]B. Borca, F. Calleja, J. J. Hinarejos, A. L. Vázquez de Parga, and R. Miranda, J. Phys. Condens. Matter **21**, 134002 (2009).
[40]M. Fonin, M. Sicot, O. Zander, S. Bouvron, Ph. Leicht, U. Rüdiger, M. Weser, Yu. S. Dedkov, and K. Horn, e-print arXiv:1010.1389v1 [cond-mat.mtrl-sci].
[41]I. Hamada and M. Otani, Phys. Rev. B **82**, 153412 (2010).
[42]R. Laskowski, P. Blaha, and K. Schwarz, Phys. Rev. B **78**, 045409 (2008).
[43]R. Laskowski and P. Blaha, Phys. Rev. B **81**, 075418 (2010).
[44]I. Pletikosic, M. Kralj, P. Pervan, R. Brako, J. Coraux, A. T. N'Diaye, C. Busse, and T. Michely, Phys. Rev. Lett. **102**, 056808 (2009).
[45]G. Ertl and J. Küppers, *Low Energy Electrons and Surface Chemistry*, 2nd ed. (VCH, Weinheim, 1985), chap. 9, formula (9.26), p. 228.